Synergizing pico hydel and battery energy storage with adaptive synchronverter control for frequency regulation of autonomous microgrids

Vasudevan, Krishnakumar R.; Ramachandaramurthy, Vigna K.; Venugopal, Gomathi; Guerrero, Josep M.; David Agundis Tinajero, Gibran

Published in:
Applied Energy

DOI (link to publication from Publisher):
10.1016/j.apenergy.2022.119827

Publication date:
2022

Document Version
Accepted author manuscript, peer reviewed version

Synergizing pico hydel and battery energy storage with adaptive synchronverter control for frequency regulation of autonomous microgrids

Krishnakumar R. Vasudevan[1*], Vigna K. Ramachandaramurthy[1], Gomathi Venugopal[2], Josep M. Guerrero[3], Gibran David Agundis Tinajero[3]

[1] Institute of Power Engineering, Department of Electrical Power Engineering, College of Engineering, Universiti Tenaga Nasional, Jalan IKRAM-UNITEN, 43000 Kajang, Selangor, Malaysia.

[2] Department of Electrical and Electronics Engineering, Anna University, Chennai, 600025, India.

[3] Department of Energy Technology, Aalborg University, Aalborg, Denmark-9220.

Abstract: The proliferation of renewable energy sources in autonomous microgrids has led to the deterioration of system inertia. In the past decade, the decrease in system inertia was addressed through numerous virtual synchronous generator (VSG) topologies. Synchronverter is one such control technique exhibiting promising performance as that of synchronous machines (SMs). Recently, myriad other modifications were carried out to enhance the capability of the synchronverter for better dynamic response. However, the limitations of fixed virtual inertia and damping coefficient were left untouched, which can be optimized for better frequency regulation of microgrids. Hence, this paper proposes an adaptive synchronverter (ASV) by optimizing OSV parameters through fuzzy logic. Subsequently, the proposed ASV was employed to control a novel pico hydel and battery hybrid energy storage for frequency regulation of the microgrid. The small-signal model of parallel operating ASVs is presented along with the eigenvalue analysis to prove the system stability under parameter variation. The MATLAB/Simulink simulation results revealed that the proposed ASV exhibited a lower rate of change of frequency and frequency nadir compared to the original synchronverter (OSV) and vector control (VC).

Keywords: Frequency regulation, Fuzzy logic, Hybrid energy storage, Pumped hydro storage, Synchronverter, Virtual synchronous generator.

Nomenclature

ASV	Adaptive synchronverter
ESS	Energy storage systems
FFT	Fast Fourier Transform
FIS	Fuzzy inference system
FLC	Fuzzy logic controller
FN	Frequency nadir
GCC	Grid connection converter
HESS	Hybrid energy storage
MCC	Machine control converter
NH	Negative high
NL	Negative low
NM	Negative medium
OSV	Original synchronverter
PAT	Pump as turbine
PH	Positive high
PHES	Pico hydel energy storage
PHS	Pumped hydro storage
PL	Positive low
PLL	Phase locked loop
PM	Positive medium
PMSM	Permanent magnet synchronous machine

* Corresponding author email address: vasudevkrishna.ceg@gmail.com (K. R Vasudevan)

RES	Renewable energy sources
ROCOF	Rate of change of frequency
SC	Supercapacitor
SM	Synchronous machine
VC	Vector control
VSC	Voltage source converter
VSG	Virtual synchronous generator
WTG	Wind turbine generator
ZE	Zero

1. Introduction

Access to clean and affordable electricity is critical for developing remote communities around the globe, and it is the 7th United Nations Sustainable Development Goal (SDG7). However, the grid supply to such secluded places is limited by rough terrain, high grid extension costs, and scattered settlements. Having said that, autonomous microgrids comprising renewable energy sources (RES) can be a sustainable alternative to grid connection. However, low inertia, poor power quality, stochastic power variations, uncertain voltage, and frequency profiles are a few bottlenecks that should be addressed for its stable operation. Hence, such microgrids mandate energy storage systems (ESS) or backup systems (diesel generators) to mitigate the aforementioned challenges. Furthermore, a sustainable ESS developed from the local energy carriers is a boon to operating the microgrid with enhanced stability [1]. Pico hydel energy storage (PHES) is an ESS developed from well irrigation systems deployed around the globe, which is investigated in this research for its application in microgrids. It is a downsized pumped hydro storage (PHS) with significant storage autonomy, a long lifetime, and low life cycle costs than lead-acid batteries [2].

Besides the numerous advantages of PHES, it suffers a few limitations: (i) limited size of the upper reservoir, (ii) incapable of toggling between pumping and generation modes instantly, and (iii) slower response. Such ESS limitations have led to the concept of hybrid energy storage systems (HESS), whereby two or more ESS are aggregated together to complement each other. The most popular hybrid pair for power system applications is the BESS-supercapacitor (SC) [3,4], while various other combinations like BESS-flywheel [5], BESS-SC-flywheel [6], BESS-Super conducting magnetic energy storage [7] were explored recently. It should be noted that the principal objective of such hybridization was to enhance the service time of BESS by exploiting the relatively faster ESS. However, the possibility of hybridizing PHS with another storage was unexplored, while this alternative is researched in this paper. Thus, a battery energy storage system (BESS) was integrated with PHES in this research, whereas other ESS can be hybridized with PHES in the future.

Rotor inertia of synchronous machines (SM) is a critical factor that holds the frequency and rotor angle stability of the power system. However, inertia deteriorates in an environment where static power converters outnumber the SMs [8] and a few aftermaths of low inertia are: (i) poor frequency and rotor angle stability, (ii) steep rate of change of frequency (ROCOF), and (iii) increased frequency nadir (FN). One such event happened on 28th September 2016 in South Australia, when two powerful tornados tore apart two main transmission lines of the state, which led to the islanding of South Australia and consequent blackout. Further investigations unveiled that the low system inertia owing to the high share of RES led to steep ROCOF and subsequent maloperation of under frequency load shedding control [9]. Hence, virtual inertia emulation techniques are imperative in the power system where the RES integration is increasing steeply and in the autonomous microgrids.

Multiple virtual synchronous generator (VSG) topologies underpinned by the swing equation were proposed to replicate the physical behaviour of SM [10]. Eventually, original synchronverter (OSV) technology was developed, and by far, it is the closest resemblance to SM [11,12]. The swing equation of the electromechanical system indicated that the dynamic frequency variation of SM depends on its rotor inertia. Similarly, it also affects the dynamic performance of VSG and synchronverter, while as a bonus, it can be tuned to meet the system requirements. Online optimization of virtual inertia will produce high inertia during frequency deviation and low inertia during frequency recovery, which is the fundamental concept of adaptive frequency control. Recently, the swing equation was modified to express inertia as the sum of constant and dynamically varying inertia components [13]. The dynamic component was defined as the first derivative of the angular speed of VSG, and it operates during system transients. Similarly, the virtual inertia component was expressed as the sum of steady-state inertia and the dynamic component, which varies based on the direction of frequency change and ROCOF [14]. In another study, the virtual rotating mass of the SV was split into three parallel rotating masses to interface type 4 wind turbine generators (WTGs) [15]. The three rotational masses have distinct roles to play: (a) take care of transient components, (b) preserve the properties of OSV and (c) increase the inertia of the system. Meanwhile, an inertia matching strategy was proposed by equating the adjustment coefficient to the droop coefficients of parallel operating VSGs. However, the validity of the proposed strategy was limited to VSGs of the same capacity, and the variation of inertia was discrete. Similarly, a coordinating adaptive virtual inertia

control was proposed to control the interlinking converters of ac-dc microgrids [16]. The virtual inertia component was varied as a hyperbolic tangent function (*tanh*) based on the direction of frequency variation.

Besides modifying the swing equation or affecting the inertial component of VSGs, intelligent techniques can also solve the purpose [17]. Although heuristics and meta-heuristics can yield accurate parameters [18], their computational delay would not positively influence the system's dynamic response. In such an instance, fuzzy logic can deliver optimal performance without the exact system model, and hence they are extensively adopted for VSG applications [19]. A fuzzy logic controller (FLC) was proposed to control type 3 and type 4 WTGs with the adaptive virtual inertia of VSG [20]. Nevertheless, the input to the FLC does not account for a critical parameter ROCOF. Likewise, another FLC was developed to optimize the virtual inertia of weak microgrids in real-time [21]. However, the phase-locked loop (PLL) was adopted to feed the frequency signal back to the system, and it may lead to PLL instability. In another study, a fuzzy secondary controller was proposed with adaptive inertia control of VSG [22]. However, the linguistic variables in [20–22] were only limited to three, which may not produce nearly optimal values.

Apart from inertia, the damping coefficient also plays a vital role in the system response speed and varying it will affect the steady-state system response. In the aforementioned studies [13–15,18–22], only the inertial component was optimized while leaving the damping coefficient untouched. Meanwhile, only a few modifications have been made to enhance the performance of OSV ever since its development [23]. The addition of a damping correction branch decoupled the droop and damping coefficients of OSV [24]. The first derivative component of torque was added to OSV's real power loop to act during system transients while preserving the steady-state droop characteristics. Similarly, a PI controller was augmented in parallel with the damping loop of OSV to zero down the steady-state error in power [24]. Furthermore, the general integrator in the real power loop of OSV was replaced with the derived bounded integral controller [25]. The proposed bounded integral controller was intended to attenuate the frequency of a weak grid.

Thus, with the above discussion, it is evident that there is a research gap to simultaneously optimize the virtual inertia and damping coefficient of OSV based on the grid frequency variations. It should also be noted that the previous works were focused on improving the VSG itself or its applications in RES. Thus, to the authors best knowledge, the PHES-BESS hybrid employing parallel adaptive synchronverters (ASVs) for frequency regulation of microgrids is yet to be reported in the literature. The main contributions of this paper are:

1. A hybrid energy storage with PHES and BESS controlled by parallel operating ASVs is proposed to support a remote microgrid. Meanwhile, the need for secondary energy storage is explained by decomposing the solar PV and PHES output into different frequencies using Fast Fourier Transform (FFT) analysis.
2. An ASV control is proposed by optimizing the virtual inertia and damping coefficients of OSV using FLC for adaptive frequency regulation of the proposed microgrid.
3. A small-signal model is presented for the proposed HESS with parallel operating ASVs and the stability of the system is assessed through eigenvalue analysis. Furthermore, the proposed strategy is compared to vector control (VC) and OSV through time-domain simulations in MATLAB/Simulink.

This paper is structured into seven sections as follows: Sections 2 and 3 present the microgrid structure and the dynamics of OSV. The proposed adaptive synchronverter control is detailed in section 4, and its stability assessment is explained in section 5. Eventually, the system performance is analyzed in section 6 and the paper is concluded in section 7.

2. Microgrid with Hybrid Energy Storage System

2.1 Microgrid configuration

The proposed microgrid is constituted of a solar PV plant, PHES, BESS, and residential loads (Fig 1). It was developed to power the remote communities involved in agricultural activities with facilities to establish PHES. A 44 kWp solar PV plant was designed to satisfy the base load of the microgrid. It was interfaced into the microgrid by a boost converter controlled by a maximum power point tracking algorithm and a voltage source inverter controlled by VC. The detailed modelling of solar PV, PHES, and BESS are not presented here to confine the scope of this article. Albeit a brief description of the interconnection and converter topologies is introduced in the subsequent sections.

2.2 Hybrid energy storage system

PHES is a downscaled PHS developed with a single pump as a turbine (PAT) with a capacity of 5 kW and 18 kWh. Its main components include a permanent magnet synchronous machine (PMSM), hydraulic governor, upper and lower reservoirs. The hydraulic governor has a tuned PI controller and a servo mechanism, which controls the discharge rate of water impinging the

PAT. The PI controller acts on the error between the desired power output and the actual power output of PHES and works to minimize the error. However, it does not affect the pumping operation since a separate outlet pipe delivers water to the upper reservoir. A two-stage voltage source converter (VSC) topology was used to operate PHES at variable speeds and control power exchange with the microgrid. Among the two converters, the machine control converter (MCC) was controlled by VC, whereas the grid connection converter (GCC) was controlled with the proposed ASV. The readers are guided to the previous article of the authors [26] for detailed modelling and description of PHES with OSV. A 5 kW-5 kWh BESS was employed to support the relatively slower PHES, thus forming the HESS. The first principle model with an ideal dc source and an internal resistance was used to model the BESS [27]. It acts as the grid forming unit by issuing the frequency and phase angle references with the proposed ASV control strategy. Notably, BESS contributes to system stability by mitigating the high-frequency power variations, while PHES caters to the long-term energy storage of the microgrid.

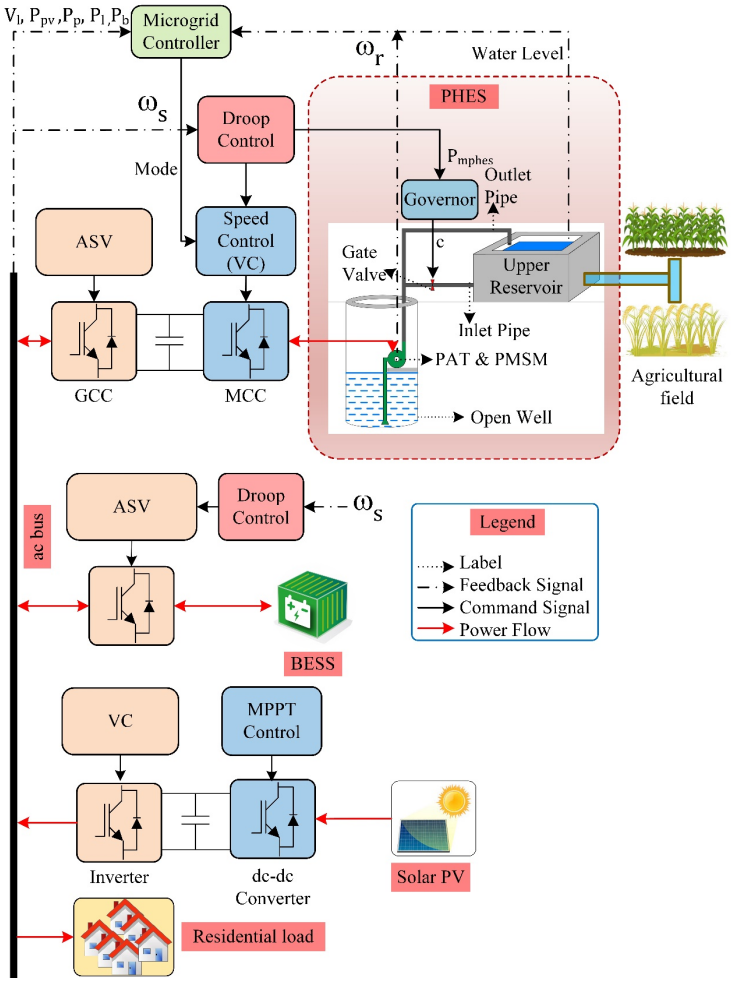

Fig 1. Proposed microgrid configuration with solar PV, PHES and BESS.

2.3 Need for hybrid energy storage system

Although PHES can support the intermittency of solar PV and meet the nocturnal demand, it has a few limitations.

(i) The energy storage autonomy is proportional to the size of the upper reservoir. However, the upper reservoir capacity is limited by the water availability in the well and constructional limitations. For instance, considering an open well size of 30 m deep and 5 m radius can hold 1570 m3 of water to its brim. However, it is practical to consider 50% of

the total volume, which is 785 m^3. Next, using the volume equation, it was computed that every kWh of energy storage requires 20.5 m^3 of water in the upper reservoir [28]. Thus, the size of the upper reservoir cannot be increased infinitely.

(ii) Instantaneous switching between the generation and pumping modes is impossible due to the use of a single PAT. The PAT should halt and reverse its rotational direction to switch between the two operating scenarios (generation and pumping). The braking and direction reversal operation of PHES has a higher mechanical time delay, which is inadequate for frequency control. Thus, a sudden change between excess generation and deficit generation cannot be handled by PHES solely.

(iii) PHES cannot handle the high-frequency power variations caused by intermittent solar insolation due to its inherent mechanical time delay.

While the first two limitations are trivial, the third limitation is detailed by decomposing the steady-state power output of solar PV and PHES into different frequencies using FFT. The power output of solar PV was obtained with a constant irradiation input of 800 W/m^2 to the simulation model. As a result, the frequency spectrum shown in Fig 2 revealed the presence of low and high-frequency components present below and above the fundamental frequency in the power output of solar PV, respectively. Furthermore, the power output of PHES was obtained from the simulation model for a discharge value of 0.02 m^3/s. Subsequently, decomposing the PHES power output into the frequency spectrum exhibited the existence of low-frequency components and the magnitude of high-frequency components was low, as shown in Fig 3. Thus, a BESS with relatively lower energy capacity was aggregated with PHES to develop a HESS, which alleviated the limitations mentioned above.

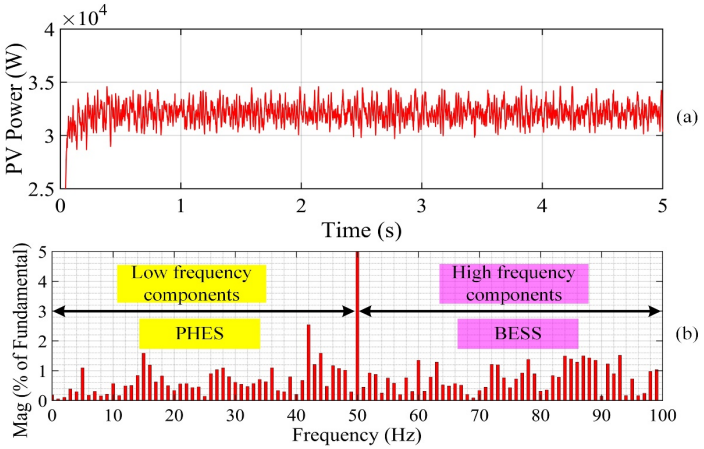

Fig 2. FFT analysis of solar PV output: (a) power output, (b) frequency spectrum.

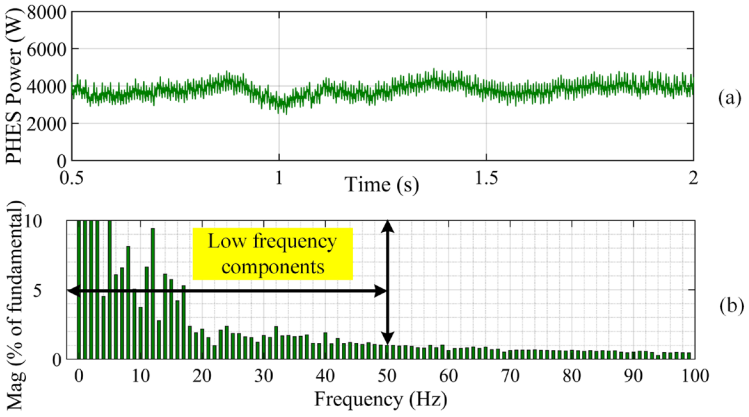

Fig 3. FFT analysis of PHES output: (a) power output, (b) frequency spectrum.

3 Original Synchronverter

3.1 Fundamentals of the original synchronverter

OSV is constituted by an ESS, a power converter, and a control algorithm developed upon the fundamentals of an SM. The modelling technique assumes a single-pole round rotor with distributed winding while neglecting the effects of magnetic saturation and damper windings. The detailed analytical modelling of OSV requires a fair knowledge of the machine dynamics, and it can be found in reference [12]. The OSV control technique utilizes two separate loops for the real and reactive power controls, as shown in Fig 4. Furthermore, it was justified that the real, reactive power loops are independent and there are no interactions between them [12]. Hence, it is fair to consider that the dynamics of the reactive power loop are constant as frequency variation is affected only by the real power exchange with the grid.

In the previous work, the OSV control was modified by augmenting a dc link voltage controller to the real power loop, which was employed to control PHES in an autonomous microgrid [26]. The dc link voltage controller issues reference torque command to the inner inertial control of the real power loop to maintain a constant dc link voltage. The variation in dc link voltage leads to a change in the synchronverter angle, which controls the power output of PHES. The control action results in the manipulation of power flow across the dc link capacitor, thereby maintaining the dc link voltage.

3.2 Dynamics of the original synchronverter

The dynamics of OSV in frequency regulation can be elucidated by analyzing the swing equation of electromechanical system (1), where ω_s, ω_0, J_s, P_{ms}, P_{es}, and D_p, represent OSV's angular frequency, nominal frequency (rad/s), virtual inertia (kgm^2), mechanical power (W), electrical power (W), and damping coefficient, respectively. Next, deducing the rotor angle from (1) and substituting the electrical power exchanged (2) by the OSV in (1) will yield (3), where E_s, V_l, and X_f are OSV voltage, line voltage (V), and filter reactance (Ω).

$$\frac{d\omega_s}{dt} = \frac{1}{J_s\omega_0}\left(P_{ms} - P_{es} - D_p\left(\omega_s - \omega_0\right)\right) \tag{1}$$

$$P_{es} = \frac{E_s V_l}{X_f} sin\theta_s \text{ , where } E_s = \phi_v \omega_s \tag{2}$$

$$J_s\omega_0 \frac{d^2\theta_s}{dt^2} = \left(P_{ms} - \frac{E_s V_l}{X_f} sin\theta_s\right) - D_p\left(\frac{d\theta_s}{dt} - \omega_0\right) \tag{3}$$

Assuming a small change in θ_s, and linearising (3) yielded (4)

$$J_s\omega_0 \frac{d^2\Delta\theta_s}{dt^2} = \left(-\frac{E_s V_l}{X_f}\Delta\theta_s\right) - D_p\left(\frac{d\Delta\theta_s}{dt} - \omega_0\right). \tag{4}$$

Next, expressing (4) in the standard form of the characteristic equation of the second-order system ensued (5).

$$\frac{d^2\Delta\theta_s}{dt^2} + \frac{D_p}{J_s\omega_0}\frac{d\Delta\theta_s}{dt} + \frac{E_s V_l}{X_f J_s\omega_0}\Delta\theta_s = 0 \tag{5}$$

$$s^2 + \frac{D_p}{J_s\omega_0}s + \frac{E_s V_l}{X_f J_s\omega_0} = 0 \tag{6}$$

Subsequently, equating the coefficients of (6) to the generalized second-order equation will give the natural frequency of oscillation (ω_n) (7) and the damping ratio (ξ) (8).

$$\omega_n^2 = \frac{E_s V_g}{J_s \omega_0 X_f} \Rightarrow \omega_n = \sqrt{\frac{E_s V_g}{J_s \omega_0 X_f}} \tag{7}$$

$$2\xi\omega_n = \frac{D_p}{J_s \omega_0} \Rightarrow \xi = \frac{D_p}{2}\sqrt{\frac{X_f}{E_s V_g J_s \omega_0}} \tag{8}$$

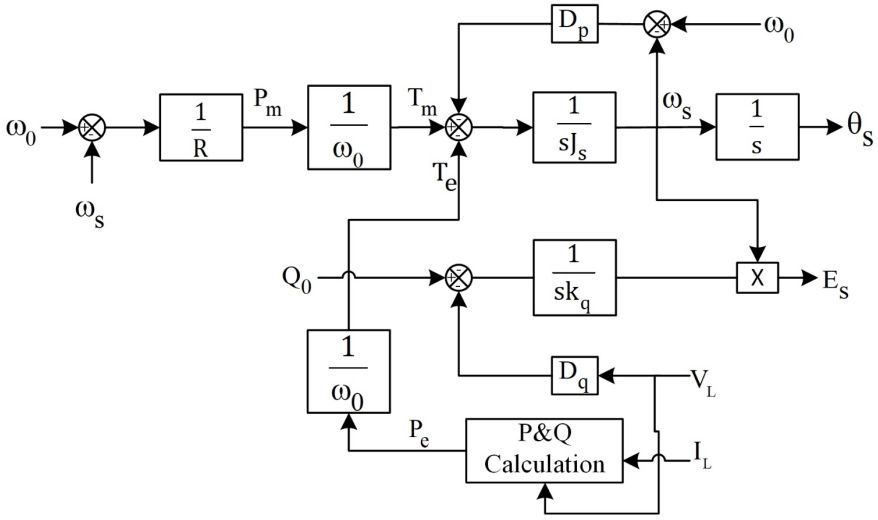

Fig 4. Original synchronverter control strategy with fixed damping coefficient and virtual inertia.

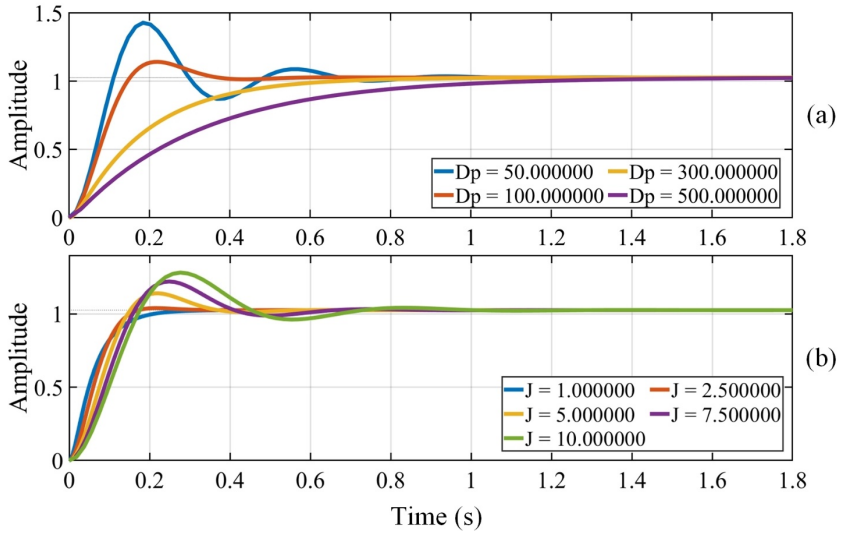

Fig 5. Unit step response for variation in (a) damping coefficient (b) virtual inertia.

It is evident that the damping ratio is proportional to D_p and has an inverse relation with J_s. The step response of (6) was evaluated by separately varying D_p and J_s to study the effect of each variable. While varying D_p from 50 to 500, an increase in the damping ratio was observed (Fig 5.(a)). Notably, at a lower value of 50, the peak overshoot reached 140% of the nominal value, and the system was underdamped. However, D_p does not affect ω_n and cannot be varied independently due to the local grid code requirements [24]. Hence, optimizing D_p to act during system transients while preserving the steady-state droop characteristics would be a better alternative over other augmented control loops. Similarly, varying J_s corroborated its inverse relationship with ξ (Fig 5.(b)). The lower values of J_s exhibited better damping over the large values, while below 1 kgm^2, the change in damping was negligible. Thus, both D_p and J_s should be dynamically changed for better frequency regulation.

4 Proposed adaptive synchronverter control

4.1 Adaptive frequency control

The instantaneous frequency of the power system is determined by the swing equation of rotating machines, as presented earlier. In a nutshell, system inertia is the ability of the SM to resist its speed change during a grid event (small or large disturbances). Consequently, the frequency deviation is restrained by exchanging the kinetic energy of the rotor with the grid. The large interconnected power systems dominated by SM have high inertia relative to small microgrids powered by RES. Albeit, the low inertia of the microgrid results in aggravated frequency deviations and sharp ROCOF, which will degrade the system's frequency profile. Thus, the deterioration of system inertia compelled researchers to develop new virtual inertia emulation strategies. Although myriad other techniques were proposed earlier, the OSV distinguishes itself with its superior performance. The virtual inertia contributed by the ASVs of BESS and PHES adds up to the inertia of the microgrid, thus, increasing the effective inertia of the microgrid.

The system frequency response after a disturbance can be demarcated into various segments to elucidate the need for dynamic frequency control, as shown in Fig 6. After a frequency event, the frequency deviates from the nominal value (50 or 60 Hz), and that region is marked as D. Subsequently, the frequency recovers after reaching a minimum or maximum point, that region is marked as R. Meanwhile, it is evident that the dynamic frequency of the system and inertia are inversely related. A large J_s would curtail ROCOF and FN, whereas a small J_s would reduce the time taken for frequency recovery. Therefore, fixed inertia will not satisfy both the requirements for enhanced frequency regulation and D_p should also be optimized along with J_s.

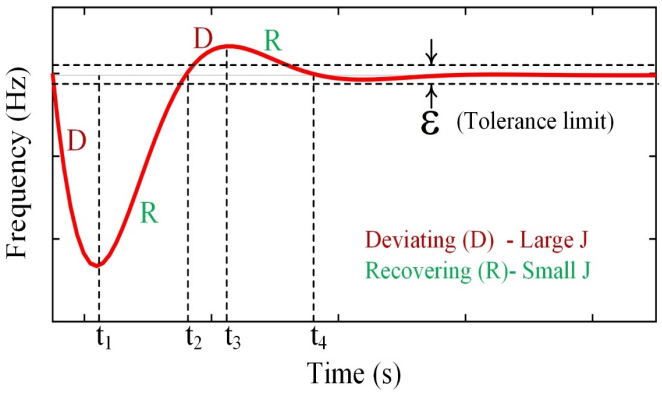

Fig 6. Frequency response curve-demarcated by different regions.

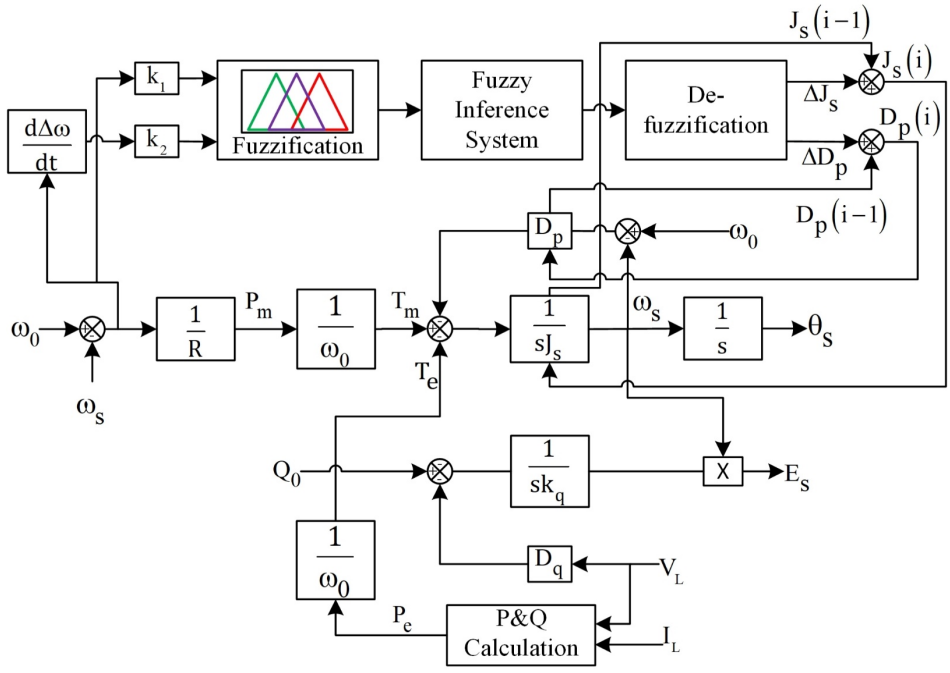

Fig 7. Proposed adaptive synchronverter control strategy with FLC.

4.2 Parameter optimization of synchronverter

The supportive arguments presented in previous sections 3.2 and 4.1 set forth the need for optimizing the OSV parameters. In such an instance, a model-independent technique like FLC would serve as a better alternative to develop the conceived ASV (Fig 7). The proposed optimization process consists of three significant steps: fuzzification, fuzzy reasoning, and de-fuzzification.

4.2.1 Fuzzification

It is the process of mapping the crisp values to the corresponding linguistic variables through membership functions. Firstly, $\Delta\omega$ and $\frac{d\Delta\omega}{dt}$ were scaled to the range [-0.5, 0.5] using the factors k_i (9) and k_j (10), respectively.

$$e_i = k_i\Delta\omega = k_i\left(\omega_s - \omega_0\right),\ \in\left[-0.5, 0.5\right] \tag{9}$$

$$e_j = k_j\frac{d\Delta\omega}{dt} = k_j\frac{d\left(\omega_s - \omega_0\right)}{dt},\ \in\left[-0.5, 0.5\right] \tag{10}$$

Following that, the triangular and Gaussian membership functions were employed to fuzzify the inputs of J_s and D_p optimization, respectively. These membership functions were defined by seven linguistic variables, which include positive high (PH), positive medium (PM), positive low (PL), zero (ZE), negative high (NH), negative medium (NM), negative low (NL) as shown in Fig 8 and Fig 9.

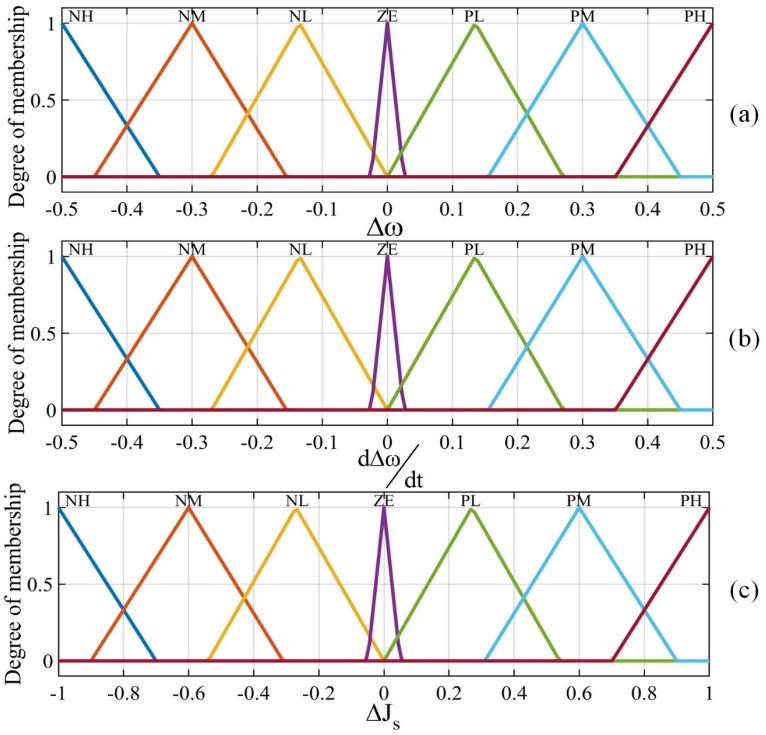

Fig 8. Membership functions for optimizing inertia (a) change in frequency, (b) rate of change of frequency (c) virtual inertia.

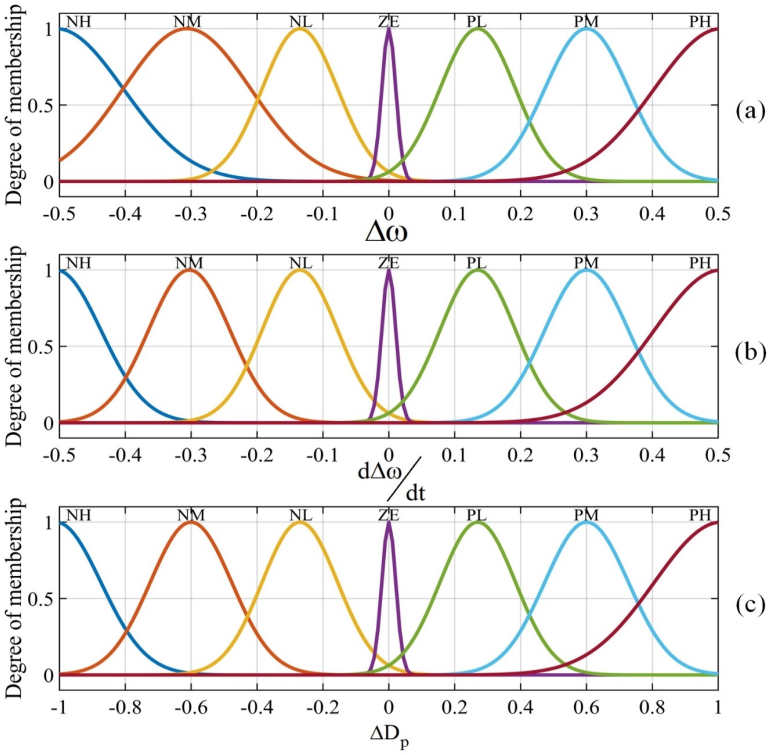

Fig 9. Membership functions for optimizing damping coefficient (a) change in frequency, (b) rate of change of frequency (c) damping coefficient.

4.2.2 Fuzzy inference system

The fuzzy inference system (FIS) maps the input variables to the output variables by utilizing the fuzzy rule base (Table A. 1 and Table A. 2). The fuzzy rules in this work were established with Mamdani FIS to meet the system requirements based on the details in section 4.1. When the frequency is deviating, e_i and e_j will have the same signs (positive or negative), which will demand an increase in J_s and D_p. Conversely, when the frequency is recovering, e_i and e_j will have opposite signs, hence, ΔJ_s and ΔD_p should decrease. For instance, a few fuzzy rules in Table 1 and Table 2 are explained as follows:

i. If e_i is PH and e_j is PH, then ΔJ_s and ΔD_p are PH. It implies that when the frequency and ROCOF deviations are large, then the change in inertia and damping coefficients are substantially increased.

ii. If e_i is PL and e_j is NH, then ΔJ_s and ΔD_p are NM. When the frequency deviation is small, and the ROCOF deviation is large in the opposite direction (negative), it implies frequency recovery. Hence, the change in inertia and damping coefficients are slightly decreased. Similarly, mapping all the other rules generated the output surfaces of ΔD_p and ΔJ_s as given by Fig 10.(a) and Fig 10.(b), respectively.

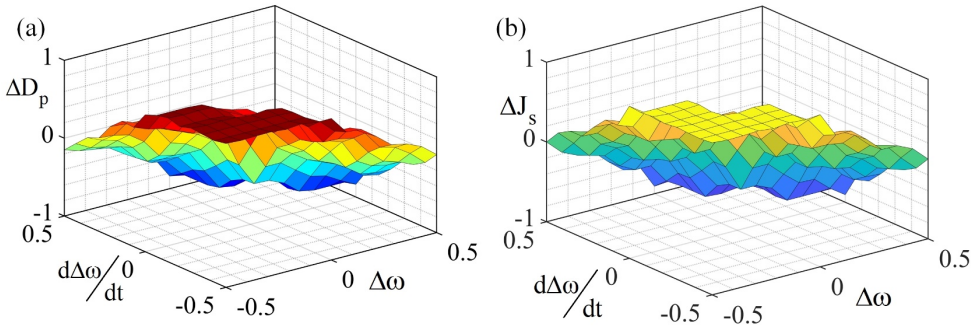

Fig 10. Output surfaces of change in (a) damping coefficient and (b) virtual inertia.

4.2.3 De-fuzzification

The outputs of FIS cannot be directly used to change the OSV parameters as they are fuzzified. Therefore, the outputs of FIS should be de-fuzzified to translate the linguistic values to crisp values of ΔJ_s and ΔD_p using various techniques. The centroid method is one such de-fuzzification technique, which was adopted in this research. It converts the linguistic value to a crisp value by computing the centroid of the fuzzy set. Firstly, the total area of the membership functions is divided into sub-areas, and then the area and centroid of each sub-areas are calculated. Finally, the summation of each sub-areas brings out the de-fuzzified crisp values. The developed ASV was employed to control both PHES and BESS for better frequency regulation.

5 Small Signal Analysis of HESS

The stability of the proposed HESS with parallel ASVs was analyzed through eigenvalue analysis of the derived small-signal model, and the results are presented in this section.

5.1 BESS-ASV

The initial step for the small-signal modelling approach was developed from the swing equation (1), and linearising it around an initial point yielded (11), where the subscript, *bess* , denotes parameters of BESS-ASV.

$$\Delta P_{mbess} - \Delta P_{ebess} = J_{bess}\omega_0 \frac{d\Delta\omega}{dt} + D_{bess}\Delta\omega \tag{11}$$

Next, a droop controller with gain, R_{bess}, was augmented to the real power loop of the OSV to derive the power reference for BESS. Linearizing the droop equation yielded, ΔP_{mbess} (12), which on substituting in (13) and applying Laplace transform generated (14).

$$\omega_s = \omega_0 - R_{bess}P_{mbess} \Rightarrow \Delta P_{mbess} = \frac{\Delta\omega}{-R_{bess}} \tag{12}$$

$$-\Delta P_{ebess} = J_{bess}\omega_s s\Delta\omega + D_{bess}\Delta\omega + \frac{\Delta\omega}{R_{bess}} \tag{13}$$

$$\Rightarrow \frac{\Delta P_{ebess}}{\Delta\omega} = -\left(J_{bess}\omega_s s + \left(D_{bess} + \frac{1}{R_{bess}}\right)\right) \tag{14}$$

Finally, inverting (14) derived the transfer function of the real power loop of the BESS ASV, where $D'_{bess} = \left(D_{bess} + \frac{1}{R_{bess}}\right)$.

$$\therefore G_{sbess}(s) = \frac{\Delta\omega}{\Delta P_{ebess}} = -\left(\frac{1}{1 + s\frac{J_{bess}\omega_s}{D'_{bess}}}\right) \tag{15}$$

5.2 PHES-ASV

An exercise similar to the previous section was carried out to derive the transfer function of the PHES ASV. However, the droop mechanism was incorporated into the hydraulic governor to control the real power, unlike the BESS control. On the other hand, the ASV was utilized to control the dc-link voltage by maintaining the real power balance across it. Firstly, the transfer function of the PHES ASV (16) was derived from the linearised droop equation, where G_{sphes} is the transfer function of the PHES-ASV control loop.

$$\omega_s = \omega_0 - R_{phes}P_{mphes} \Rightarrow \Delta\omega = -R_{phes}\Delta P_{mphes} \cdot G_{sphes} \tag{16}$$

The power reference to PHES does not instantly translate to the change in output power, so the droop function was expressed as the function of governor time delay (17), where R_{phes} is the droop coefficient of PHES.

$$R_{phes}(s) = \left|R_{phes}\right|\left(\frac{1}{1 + s\tau_g}\right) \tag{17}$$

Notably, the OSV control was modified by adding a dc link voltage controller with a transfer function, $G_{vdc}(s)$, to the torque control loop with a transfer function, $G_{torque}(s)$, for regulating the dc link voltage of PHES (v_{dc}^{p}) (18). Next, the synchronizing

torque loop, $G_{sync}(s)$, with power coefficient, K_{sync}, was utilized to convert the synchronverter angle to dc link voltage. Eventually, the final transfer function (21) was derived by inserting (20) in (16).

$$G_{sphes}(s) = G_{vdc}(s) \cdot G_{torque}(s) \cdot G_{sync}(s) \tag{18}$$

$$G_{sphes}(s) = \left(\frac{s}{K_{iv} + sK_{pv}}\right) \cdot \left(\frac{1}{D_{phes} + sJ_{phes}}\right) \cdot \left(\frac{1}{s}\right) \cdot \left(\frac{K_{sync}}{v_{dc}^{0}\left(C_{phes}s + q_p\right)}\right) \tag{19}$$

$$G_{sphes}(s) = \frac{K_{syn}}{v_{dc}^{p}} \left(\frac{1}{\alpha s^3 + \beta s^2 + \gamma s + \chi}\right) \tag{20}$$

where, $\alpha = J_{phes}C_{phes}$, $\beta = C_{phes}\left(K_{iv}J_{phes} + K_{pv}D_p + J_{phes}q_p\right)$, $\gamma = C_{phes}\left(K_{iv}D_{phes} + J_{phes}K_{iv}q_p + K_{iv}D_{phes}\right)$, $\chi = C_{phes}K_{iv}D_{phes}$.

$$G_{phes}(s) = -\left|R_{phes}\right| \left(\frac{K_{syn}}{v_{dc}^{p}}\right) \frac{1}{\left(\alpha s^3 + \beta s^2 + \gamma s + \chi\right)\left(1 + s\tau_{gov}\right)} \tag{21}$$

Eventually, the system's stability was analyzed by integrating the small-signal models of BESS ($G_{bess}(s)$) and PHES ($G_{phes}(s)$) fed by ASVs using (22).

$$G_{system}(s) = G_{bess}(s) - G_{phes}(s) \tag{22}$$

5.3 Stability analysis

The sensitivity of the system to virtual inertia and damping coefficients of both the ASVs was analyzed by tracing the loci of their eigenvalues. Fig 11.(a) and Fig 11.(b) indicate the eigenvalue loci obtained by varying $D_{bess} \in [10,1000]$ and $J_{bess} \in [0.1,10]$, respectively. The conjugate pole λ_1 moved towards the origin, and the oscillation frequency increased in the beginning and started to decrease beyond a certain value when D_{bess} (J_{bess} =5 kgm^2) was varied (Fig 11.(a)).

Meanwhile, varying J_{bess} (D_{bess} =300) exhibited a similar response; however, the conjugate pole λ_1 moved towards the origin with an increased oscillation frequency (Fig 11.(b)). Subsequently, varying the parameters of PHES-ASV ($D_{phes} \in [10,1000]$, $J_{phes} \in [0.1,10]$) offered a similar response to BESS-ASV. When D_{phes} was varied (J_{phes} =5 kgm^2), the conjugate pole λ_1 moved close to the origin with an initial increase in oscillation frequency, which decreased after D_{phes} = 500 (Fig 11.(c)). Next, varying J_{phes} (D_{phes} = 300) yielded a trace where the conjugate pole λ_1 approached the origin, and the oscillation frequency was increased (Fig 11.(d)). The eigenvalue traces presented here indicates that the poles did not enter the right side of the s-plane for the considered scenarios and thus ensuring system stability. However, for further increase in , J_{phes} and J_{bess}, beyond 10 kgm^2, the eigenvalues would enter the right half of the s-plane. Hence the values of, J_{phes} and J_{bess} are limited to 10 kgm^2 and this exercise has also dictated the range of D_{phes} and D_{bess} .

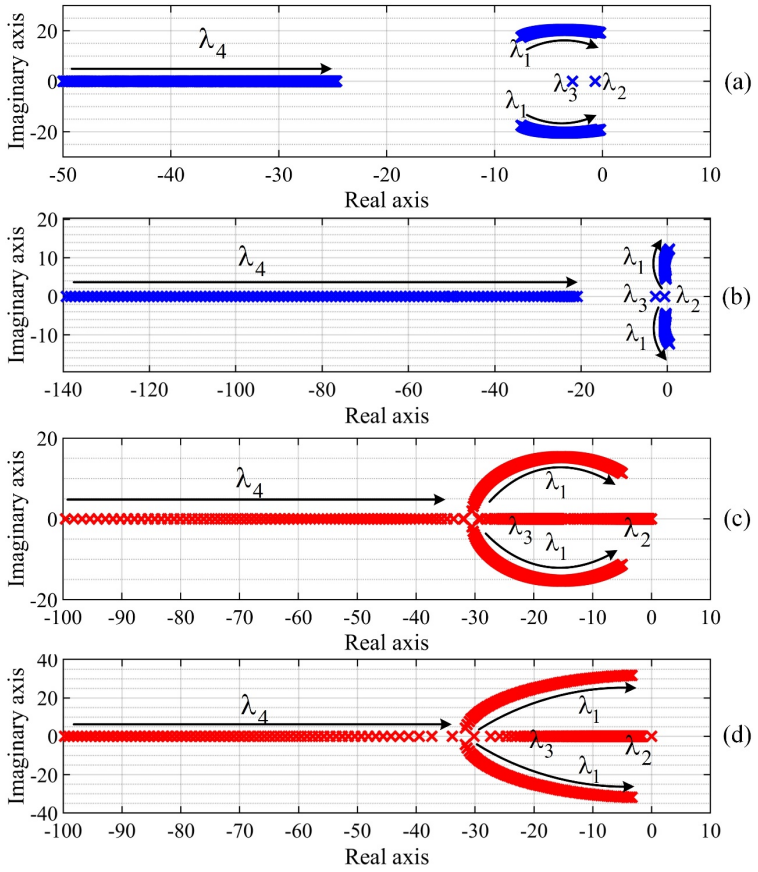

Fig 11. Eigenvalue loci for variation in (a) D_{bess} ,(b) J_{bess} ,(c) D_{phes} ,(d) J_{phes} .

6 Performance Assessment

The results of time-domain simulations were utilized to assess the performance of the proposed ASV strategy by considering frequency metrics such as ROCOF and FN under three-phase fault, load and irradiation changes. The G59 guidelines issued by the Energy Networks Association, UK, dictate the maximum ROCOF of 0.5 Hz/s and the frequency deviation of 50±1.5 Hz [29,30]. Thus, the anticipated ROCOF and frequency deviation in the proposed microgrid should be within the indicated range and it was used to benchmark the proposed ASV strategy.

6.1 PHES in generation operation

6.1.1 Fault analysis

Once the system reached steady-state, a three-phase to ground fault was simulated at t=2 s at the ac bus. The system frequency response can be observed in Fig 12.(a), and it shows that the FN was minimum (49.98 Hz) with ASV as opposed to 49.83 Hz with OSV. However, VC offered a poor response with a maximum FN= 49.58 Hz, owing to its zero inertial capability. Meanwhile, the ROCOF characteristics exhibited a similar response to the frequency, where ASV showed a minimum ROCOF=0.3 Hz/s and OSV indicated ROCOF=1 Hz/s, as observed in Fig 12.(b).

In comparison, VC exhibited an inadequate response with a maximum ROCOF= 2.4 Hz/s. The dynamic variation of J_s and D_p by the FLC is the underlying reason for the superior performance of ASV. Observing Fig 12.(c) and Fig 12.(d) revealed that, initially, the ASV parameters were J_s = 4.95 kgm^2 and D_p = 300. They were steadily increased to 9 kgm^2 and 400,

respectively, to curtail the frequency deviation after the fault. The power share of various entities in the microgrid is depicted in Fig 13. Fig 13.(a) shows that the irradiation was maintained at 800 W/m^2 to simulate the fault and analyze the transient response of the system. The total load connected was 35 kW, out of which the solar PV met 31 kW, which are presented in Fig 13.(e) and Fig 13.(d). Simultaneously, Fig 13.(c) and Fig 13.(b) indicate that PHES and BESS catered to the deficit of 4 kW by injecting 3.5 kW and 0.5 kW, respectively. It should be noted that the proposed ASV restricted the ROCOF below 0.5 Hz/s and the FN within 50±1.5 Hz in both the scenarios considered in the generation operation of PHES. Meanwhile, BESS controlled by ASV had minimum steady-state power offset as opposed to OSV and VC.

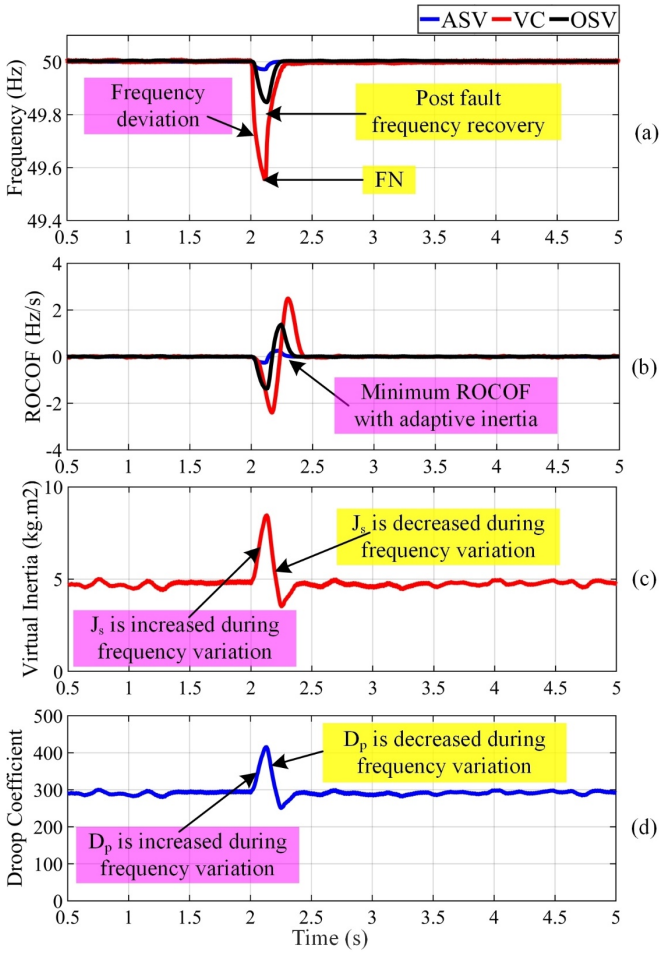

Fig 12. System performance in PHES generation mode under three-phase fault: (a) frequency, (b) ROCOF, (c) optimized virtual inertia and (d) optimized damping coefficient.

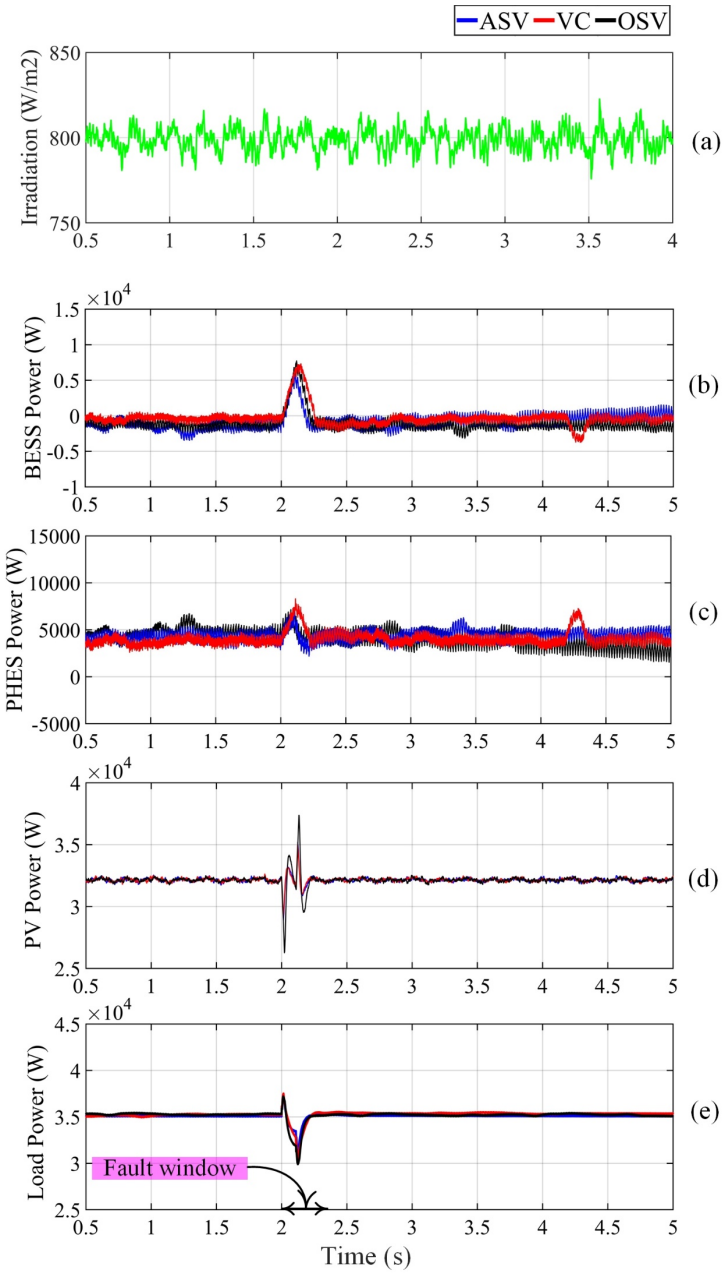

Fig 13. Power share in PHES generation mode under three-phase fault: (a) solar irradiation (b) BESS power, (c) PHES power, (d) Solar PV power, and (e) load power.

6.1.2 Load and irradiation change

The load switching and irradiation change transients were induced to the system for analyzing the system stability after the steady-state was attained (Fig 14). The irradiation input to the solar PV was levelled at a mean value of 800 W/m^2, generating 32.5 kW, as shown in Fig 15.(a) and Fig 15.(d). The load was held constant at 35 kW and PHES compensated a deficit of 2.5 kW, as illustrated in Fig 15.(e) and Fig 15.(c), while BESS absorbed the high-frequency power variations, as shown in Fig 15.(b). The load was increased from 35 kW to 40 kW at t=2 s to realize the first transition, leaving a deficit of 7.5 kW. The load transition led to a spontaneous response by BESS, which injects 2.5 kW, while PHES catered to the major portion of 5 kW. The first transition led to an under-frequency event owing to the shortage in power, which can be observed in Fig

14.(a). It shows that the VC has resulted in a drop in frequency from 50.02 Hz to 49.998 Hz, while no considerable change was observed with the ASV and OSV strategies. Similarly, Fig 14.(b) shows that the ROCOF was limited to 0.022 Hz/s with ASV control when compared to 0.05 Hz/s with OSV and 0.15 Hz/s with VC. However, it should be noted from Fig 14.(d) that there is a frequency offset with OSV, whereas the ASV eliminated the offset by varying D_p in real-time from 280 to 300. Similarly, the frequency dip during the first transition was minimum owing to the dynamic variation of J_s from 4.5 kgm^2 to 5.75 kgm^2, as shown in Fig 14.(c).

Next, the irradiation input to the solar PV was reduced from 800 W/m^2 to 650 W/m^2 and the load was reverted from 35 kW to 40 kW to incite the second transition at t=4 s. It resulted in the reduction of PV power generation from 32.5 kW to 26 kW. Consequently, PHES and BESS shared 5 kW and 4 kW, respectively, to meet the deficit of 9 kW from their reserve capacity. The irradiation change had a considerable impact on the system frequency with VC, while ASV and OSV did not show a conspicuous change in frequency. Similar to the previous case, the frequency offset increased with OSV due to the fixed value of D_p. However, ASV resulted in zero offset with the dynamic variation of D_p from 300 to 315.

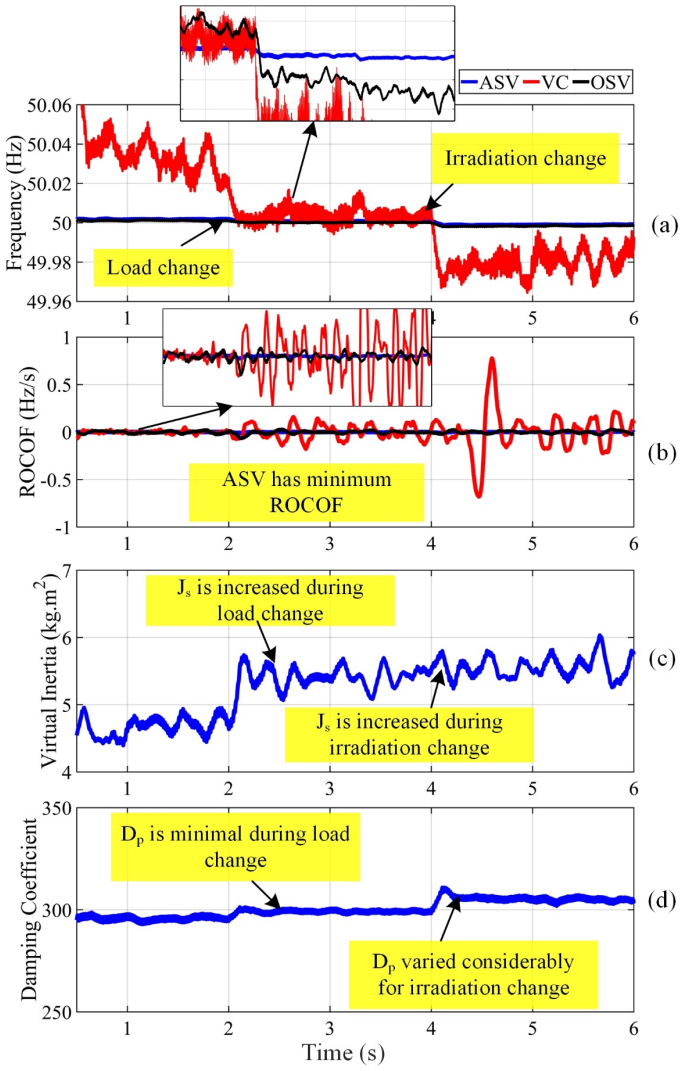

Fig 14. System performance in PHES generation mode under load and irradiance change: (a) frequency, (b) ROCOF, (c) optimized virtual inertia and (d) optimized damping coefficient.

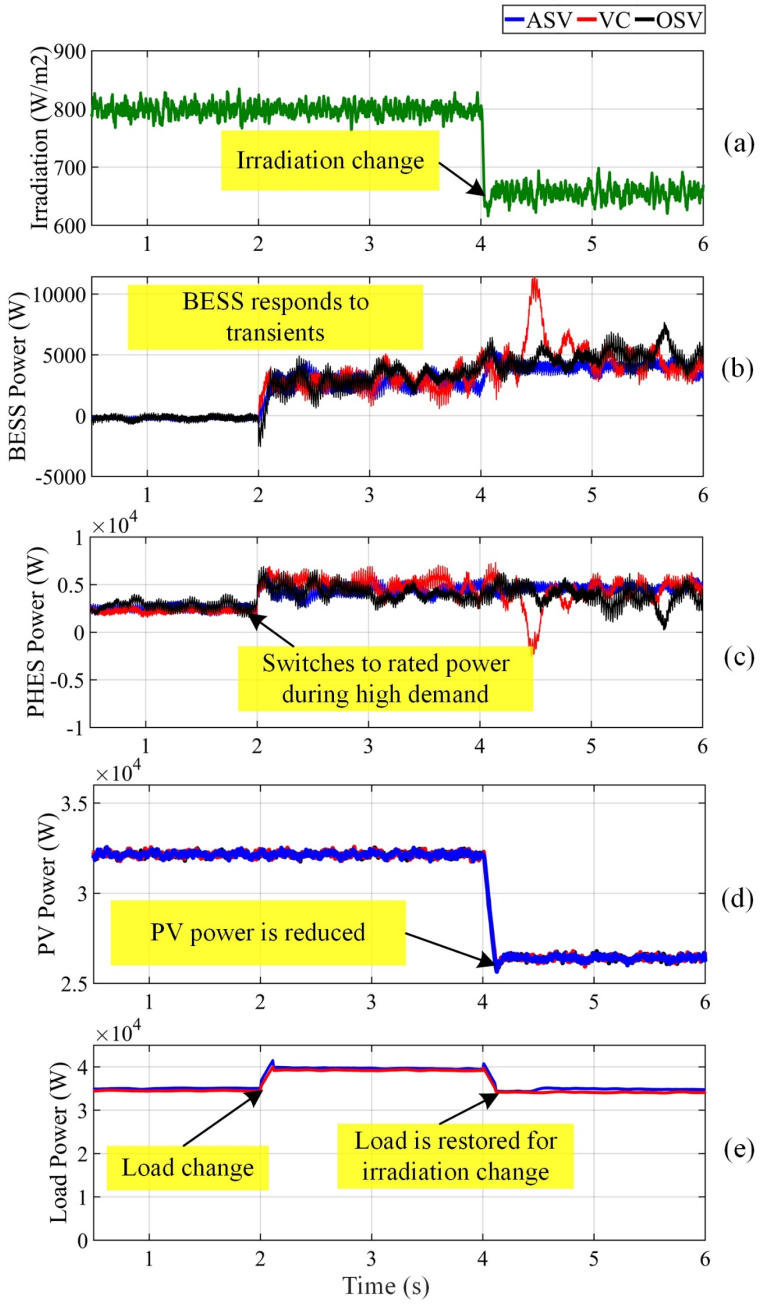

Fig 15. Power share in PHES generation mode under load and irradiance change: (a) solar irradiation (b) BESS power, (c) PHES power, (d) Solar PV power, and (e) load power.

6.2 PHES in pumping operation

6.2.1 Fault analysis

In this case, excess solar PV generation was absorbed by operating PHES in pumping mode and charging the BESS. A three-phase fault was induced at the ac bus to analyze the performance under fault at t=2 s. After the fault, the ASV parameters were increased gradually from their initial values $J_s = 5$ kgm^2 and $D_p = 300$ to their peak values $J_s = 9$ kgm^2 and $D_p = 420$ to curtail the frequency deviation. The aftermath of such an exercise is the reduced FN (49.96 Hz) and ROCOF (0.5 Hz/s) with ASV compared to OSV with FN=49.82 Hz and ROCOF=1.8 Hz/s, which were inferred from Fig 16.(a) and Fig 16 .(b).

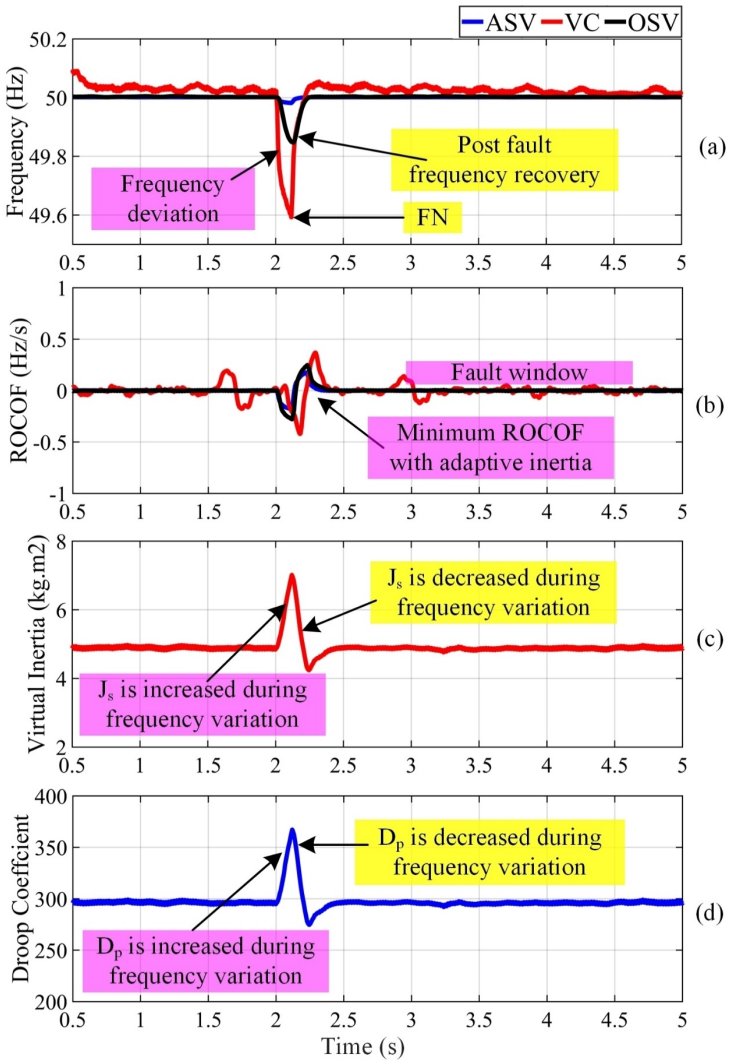

Fig 16. System performance in PHES pumping mode under three-phase fault: (a) frequency, (b) ROCOF, (c) optimized virtual inertia and (d) optimized damping coefficient.

Meanwhile, VC demonstrated a poor performance with FN=49.58 and ROCOF=2.5 Hz/s. Next, the parameters J_s and D_p were reduced to J_s = 4.25 kgm^2 and D_p = 420 to expedite the frequency recovery, as depicted in Fig 16.(c) and Fig 16.(d). Consequently, the frequency reached the nominal value at t=2.19 s, t= 2.3 s, t=2.4 s with ASV, OSV, and VC, respectively. Thus, the results substantiate the superior performance of ASV over the other two techniques for frequency regulation. Finally, the total load is presented in Fig 17.(e) and the power exchanged by BESS, PHES and solar PV are presented in Fig 17.(b), Fig 17.(c) and Fig 17.(d), respectively. The total generation by solar PV was 36 kW, whereas the net load connected to the ac bus was 26 kW. Subsequently, an excess power of 10 kW was equally consumed by BESS and PHES. It is worth noting that BESS has a power offset of 500 W with OSV versus no power offset with ASV due to the dynamic variation of D_p . Meanwhile, the proposed ASV curtailed the ROCOF within 0.5 Hz/s and maintained the FN within 50±1.5 Hz in both the cases considered in the pumping operation of PHES.

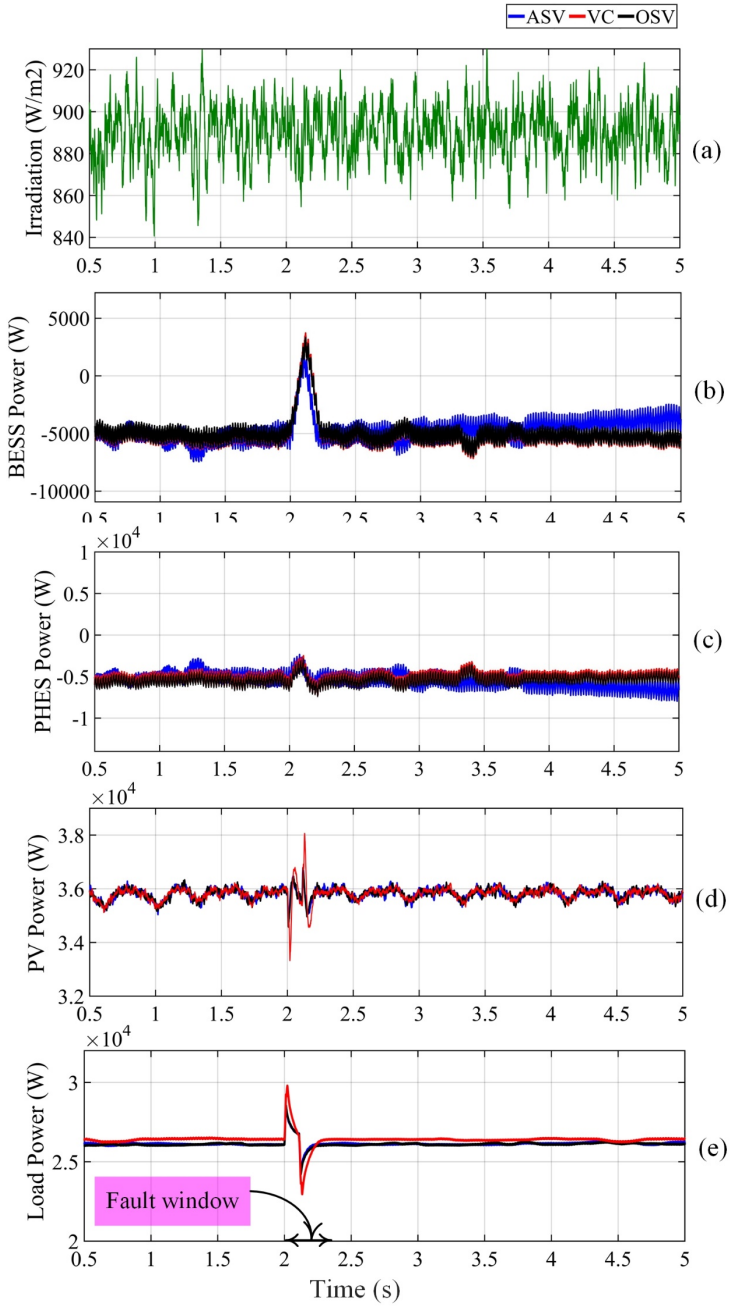

Fig 17. Power share in PHES pumping mode under three-phase fault: (a) solar irradiation (b) BESS power, (c) PHES power, (d) Solar PV power, and (e) load power.

6.2.2 Load and irradiation change

Like the generation mode, the load and irradiance were varied in real-time after the system reached steady-state (Fig 18). Initially, the irradiation input to the solar PV was 920 W/m^2, which resulted in power generation of 37.5 kW, as evident in Fig 19.(a) and Fig 19.(d). Meanwhile, Fig 19.(e) illustrates that the load connected to the microgrid was 27.5 kW leading to 10 kW surplus power in the microgrid. Fig 19.(b) and Fig 19.(c) show that both PHES and BESS consumed 5 kW each to nullify the effect of surplus power in the microgrid. The load was increased from 27.5 kW to 30 kW at t=2 s to impart the first transition and it led to a shortfall of 7.5 kW. Consequently, BESS reacted swiftly to the increase in demand and reduced its charging power from 5 kW to 2.5 kW, while the power consumption of PHES remained at 5 kW without any change.

As a result of increased demand in the microgrid at t=2 s, an under-frequency event was observed in Fig 18.(a). The VC led to a drop in frequency from 50.03 Hz to 49.998 Hz, whereas no significant change in frequency was observed with ASV and OSV. Meanwhile, ASV, OSV and VC limited the ROCOF to 0.02 Hz/s, 0.05 Hz/s and 0.2 Hz/s, respectively, as shown in Fig 18.(b). However, Fig 18.(d) is noteworthy since the frequency offset with OSV was eliminated by employing ASV, which varied D_p in real-time from 290 to 300. Likewise, it can be observed from Fig 18.(c) that the dip in frequency after the first transition was minimum, owed by the dynamic variation of J_s from 4.7 kgm^2 to 5 kgm^2.

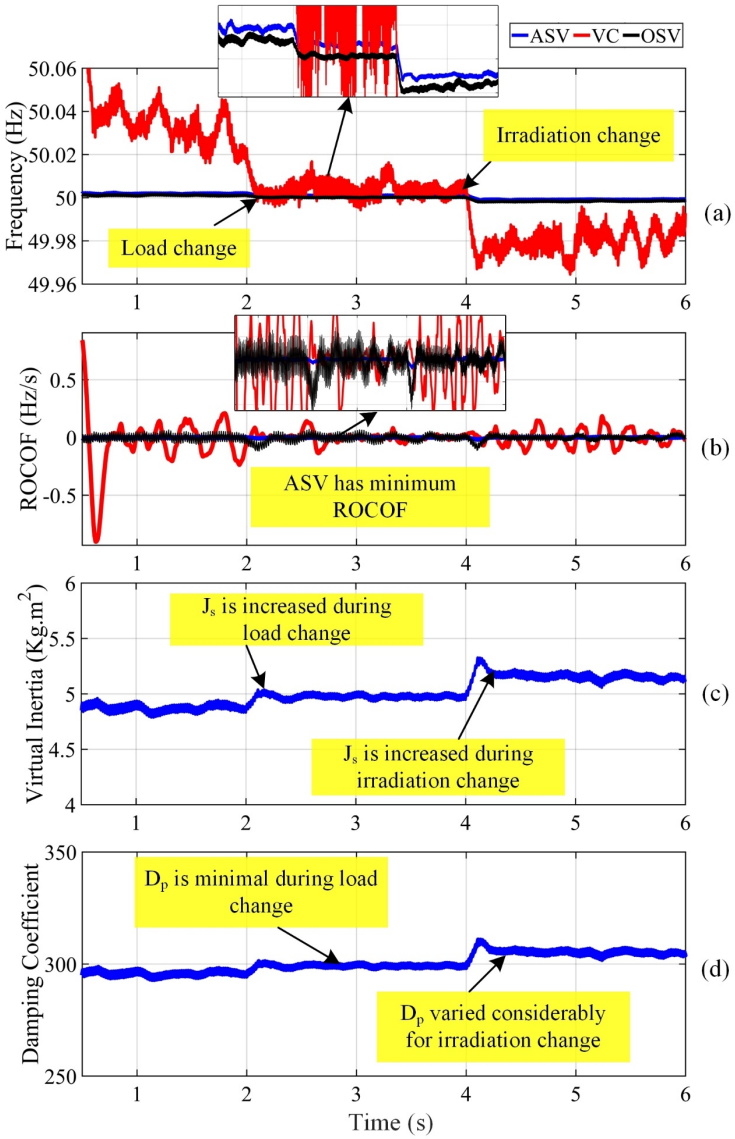

Fig 18. System performance in PHES pumping mode under load and irradiance change: (a) frequency, (b) ROCOF, (c) optimized virtual inertia and (d) optimized damping coefficient.

At t=4 s, solar irradiation was decreased from 920 W/m^2 to 720 W/m^2, which resulted in a reduction of PV power generation from 37.5 kW to 30.5 kW. The load was reduced from 30 kW to 27.5 kW to study the impact of variation in irradiation. The load switching and irradiation change exercise led to a surplus power of 3 kW, which was jointly absorbed by PHES and BESS. It is worthwhile to note that the effect of changing irradiation on frequency response was only observed with VC, whereas ASV and OSV did not exhibit significant change. Similar to the previous case, the frequency offset increased with OSV due to the

fixed value of D_p . However, ASV resulted in zero offset with the dynamic variation of D_p from 300 to 315. Meanwhile, J_s was increased from 4.7 kgm^2 to 5 kgm^2 to mitigate the transients due to the change in irradiation.

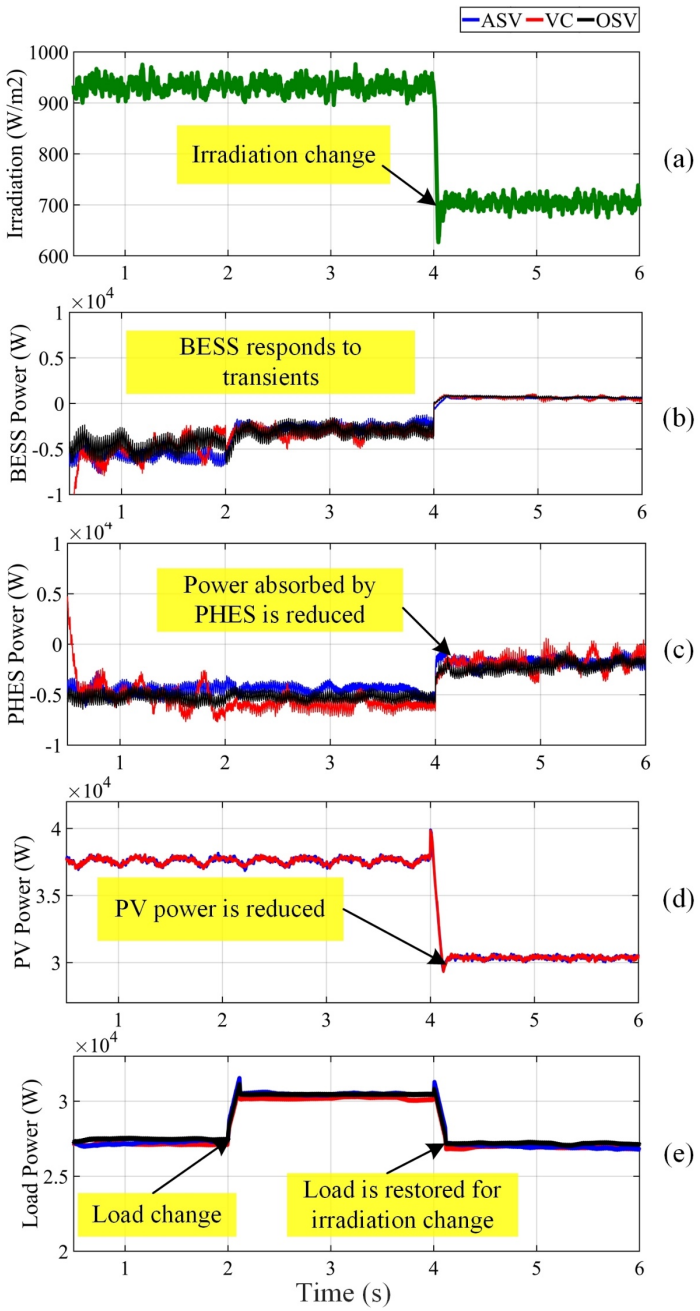

Fig 19. Power share in PHES pumping mode under load and irradiance change: (a) solar irradiation (b) BESS power, (c) PHES power, (d) Solar PV power, and (e) load power.

7 Conclusion

The primary aim of this paper was to develop an ASV to control the PHES-HESS hybrid by optimizing the virtual inertia and damping coefficient of OSV for better frequency regulation. Firstly, the need for a second ESS (BESS) was justified by decomposing the solar PV output and PHES output into the spectrum of frequency. Next, the dynamics of OSV was explained by linearising the swing equation and expressing it as a second-order system. The expressions of damping ratio and natural

frequency of oscillation revealed the correlation of system dynamics with the OSV parameters. Consequently, the ASV was proposed by optimizing the virtual inertia and damping coefficient of OSV utilizing FLC in real-time. The small-signal model of the proposed HESS was established, and its stability was proved by tracing the eigenvalues. Finally, the efficacy of the developed strategy in frequency regulation of the microgrid was elucidated through time-domain simulations. A three-phase fault was simulated at the ac bus in both the modes of operation of PHES. The frequency metrics FN and ROCOF were evaluated for the proposed ASV, and it was compared with OSV and VC. The results unveiled that the proposed ASV exhibited lower FN and gradual ROCOF by continuously varying the virtual inertia and damping coefficient. Meanwhile, the proposed ASV maintained FN and ROCOF within limits specified by G59 guidelines. Furthermore, coordination of PHES with other faster reacting ESS is worthwhile exploring in the future.

8 ACKNOWLEDGEMENT

This research was supported by "Universiti Tenaga Nasional, Malaysia, Internal Research Grant OPEX (J5100D4103-BOLDREFRESH2025-Centre of Excellence)."

9 APPENDIX

Table A. 1: Fuzzy rule base for optimizing virtual inertia

e_j \ e_i	PH	PM	PL	ZE	NL	NM	NH
PH	PH	PH	PH	PH	PM	PL	ZE
PM	PH	PH	PH	PM	PL	ZE	NL
PL	PH	PH	PM	PL	ZE	NL	NM
ZE	PH	PM	PL	ZE	NL	NM	NH
NL	PM	PL	ZE	NL	NM	NH	NH
NM	PL	ZE	NL	NM	NH	NH	NH
NH	ZE	NL	NM	NH	NH	NH	NH

Table A. 2: Fuzzy rule base for optimizing damping coefficient

e_j \ e_i	PH	PM	PL	ZE	NL	NM	NH
PH	PH	PH	PH	PH	PM	PL	ZE
PM	PH	PH	PM	PM	PL	ZE	NL
PL	PH	PM	PM	PL	ZE	NL	NM
ZE	PH	PM	PL	ZE	NL	NM	NH
NL	PM	PL	PL	NL	NM	NM	NH
NM	PL	NL	NL	NM	NM	NH	NH
NH	PL	NL	NM	NH	NH	NH	NH

References

[1] Luo X, Wang J, Dooner M, Clarke J. Overview of current development in electrical energy storage technologies and the application potential in power system operation. Appl Energy 2015;137:511–36. https://doi.org/10.1016/j.apenergy.2014.09.081.

[2] Mousavi N, Kothapalli G, Habibi D, Das CK, Baniasadi A. Modelling, design, and experimental validation of a grid-connected farmhouse comprising a photovoltaic and a pumped hydro storage system. Energy Convers Manag 2020;210:112675. https://doi.org/10.1016/j.enconman.2020.112675.

[3] Anilkumar TT, Simon SP, Padhy NP. Residential electricity cost minimization model through open well-pico turbine pumped storage system. Appl Energy 2017;195:23–35. https://doi.org/10.1016/j.apenergy.2017.03.020.
[4] Ma T, Yang H, Lu L. Feasibility study and economic analysis of pumped hydro storage and battery storage for a renewable energy powered island. Energy Convers Manag 2014;79:387–97. https://doi.org/10.1016/j.enconman.2013.12.047.
[5] Ma T, Yang H, Lu L. Development of hybrid battery-supercapacitor energy storage for remote area renewable energy systems. Appl Energy 2015;153:56–62. https://doi.org/10.1016/j.apenergy.2014.12.008.
[6] Li J, Xiong R, Yang Q, Liang F, Zhang M, Yuan W. Design/test of a hybrid energy storage system for primary frequency control using a dynamic droop method in an isolated microgrid power system. Appl Energy 2017;201:257–69. https://doi.org/10.1016/j.apenergy.2016.10.066.
[7] Khodadoost Arani AA, Gharehpetian GB, Abedi M. A Novel Control Method Based on Droop for Cooperation of Flywheel and Battery Energy Storage Systems in Islanded Microgrids. IEEE Syst J 2020;14:1080–7. https://doi.org/10.1109/JSYST.2019.2911160.
[8] Sanchez F, Cayenne J, Gonzalez-Longatt F, Rueda JL. Controller to Enable the Enhanced Frequency Response Services from a Multi-Electrical Energy Storage System. IET Gener Transm Distrib 2018;13:258–65. https://doi.org/10.1049/iet-gtd.2018.5931.
[9] Saeedian M, Pournazarian B, Taheri S, Pouresmaeil E. Provision of Synthetic Inertia Support for Converter-Dominated Weak Grids. IEEE Syst J 2021:1–10. https://doi.org/10.1109/JSYST.2021.3060866.
[10] Australian Energy Market Operator. Black System South Australia 28 September 2016. Australian Energy Market Operator; n.d.
[11] Bevrani H, Ise T, Miura Y. Virtual synchronous generators: A survey and new perspectives. Int J Electr Power Energy Syst 2014;54:244–54. https://doi.org/10.1016/j.ijepes.2013.07.009.
[12] Zhong QC, Weiss G. Synchronverters: Inverters that mimic synchronous generators. IEEE Trans Ind Electron 2011;58:1259–67. https://doi.org/10.1109/TIE.2010.2048839.
[13] Zhong QC, Ma Z, Ming WL, Konstantopoulos GC. Grid-friendly wind power systems based on the synchronverter technology. Energy Convers Manag 2015;89:719–26. https://doi.org/10.1016/j.enconman.2014.10.027.
[14] Hou X, Sun Y, Zhang X, Lu J, Wang P, Guerrero JM. Improvement of Frequency Regulation in VSG-Based AC Microgrid Via Adaptive Virtual Inertia. IEEE Trans Power Electron 2020;35:1589–602. https://doi.org/10.1109/TPEL.2019.2923734.
[15] Ren M, Li T, Shi K, Xu P, Sun Y. Coordinated Control Strategy of Virtual Synchronous Generator Based on Adaptive Moment of Inertia and Virtual Impedance. IEEE J Emerg Sel Top Circuits Syst 2021;3357:1–12. https://doi.org/10.1109/JETCAS.2021.3051320.
[16] Shi K, Chen C, Sun Y, Xu P, Yang Y, Blaabjerg F. Rotor inertia adaptive control and inertia matching strategy based on parallel virtual synchronous generators system. IET Gener Transm Distrib 2020;14:1854–61. https://doi.org/10.1049/iet-gtd.2019.1394.
[17] Zhang Y, Sun Q, Zhou J, Li L, Wang P, Guerrero JM. Coordinated Control of Networked AC/DC Microgrids with Adaptive Virtual Inertia and Governor-Gain for Stability Enhancement. IEEE Trans Energy Convers 2020;36:1–1. https://doi.org/10.1109/tec.2020.3011223.
[18] Torres L. MA, Lopes LAC, Morán T. LA, Espinoza C. JR. Self-tuning virtual synchronous machine: A control strategy for energy storage systems to support dynamic frequency control. IEEE Trans Energy Convers 2014;29:833–40. https://doi.org/10.1109/TEC.2014.2362577.
[19] Alipoor J, Miura Y, Ise T. Stability assessment and optimization methods for microgrid with multiple VSG units. IEEE Trans Smart Grid 2018;9:1462–71. https://doi.org/10.1109/TSG.2016.2592508.
[20] Thomas V, S K, Ashok S. Fuzzy Controller-based Self-Adaptive Virtual Synchronous Machine for Microgrid Application. IEEE Trans Energy Convers 2021;8969:1–1. https://doi.org/10.1109/tec.2021.3057487.
[21] Pradhan C, Narayan C, Kumar A. Adaptive virtual inertia-based frequency regulation in wind power systems. Renew Energy 2018;115:558–74. https://doi.org/10.1016/j.renene.2017.08.065.
[22] Karimi A, Khayat Y, Naderi M, Dragičević T, Mirzaei R, Blaabjerg F, et al. Inertia Response Improvement in AC Microgrids: A Fuzzy-Based Virtual Synchronous Generator Control. IEEE Trans Power Electron 2020;35:4321–31. https://doi.org/10.1109/TPEL.2019.2937397.
[23] Andalib-Bin-Karim C, Liang X, Zhang H. Fuzzy-Secondary-Controller-Based Virtual Synchronous Generator Control Scheme for Interfacing Inverters of Renewable Distributed Generation in Microgrids. IEEE Trans Ind Appl 2018;54:1047–61. https://doi.org/10.1109/TIA.2017.2773432.
[24] Dong S, Chen YC. Adjusting Synchronverter Dynamic Response Speed via Damping Correction Loop. IEEE Trans Energy Convers 2017;32:608–19. https://doi.org/10.1109/TEC.2016.2645450.
[25] Younis T, Ismeil M, Hussain EK, Orabi M. Improved single-phase self-synchronised synchronverter with enhanced

dynamics and current limitation capability. IET Power Electron 2019;12:337–44. https://doi.org/10.1049/iet-pel.2018.5582.
[26] Vasudevan KR, Ramachandaramurthy VK, Venugopal G, Guerrero JM, Ekanayake JB, Tiong SK. Variable-Speed PICO Hydel Energy Storage With Synchronverter Control to Emulate Virtual Inertia in Autonomous Microgrids. IEEE Syst J 2021:1–12. https://doi.org/10.1109/JSYST.2021.3053358.
[27] Fotouhi A, Auger DJ, Propp K, Longo S, Wild M. A review on electric vehicle battery modelling: From Lithium-ion toward Lithium-Sulphur. Renew Sustain Energy Rev 2016;56:1008–21. https://doi.org/10.1016/j.rser.2015.12.009.
[28] Krishnakumar R. V, Vigna KR, Gomathi V, Ekanayake JB, Tiong SK. Modelling and simulation of variable speed pico hydel energy storage system for microgrid applications. J Energy Storage 2019;24. https://doi.org/10.1016/j.est.2019.100808.
[29] Tamrakar U, Shrestha D, Maharjan M, Bhattarai BP, Hansen TM, Tonkoski R. Virtual inertia: Current trends and future directions. Appl Sci 2017;7:1–29. https://doi.org/10.3390/app7070654.
[30] Energy Networks Association. Engineering Recommendation G59 Issue 3 Amendment 3 2015. https://www.nationalgrid.com/sites/default/files/documents/GC0079 Annex 3 Option 1 G59 proposals 170731.pdf (accessed September 16, 2019).